Check for updates

# Bridging adsorption analytics and catalytic kinetics for metal-exchanged zeolites

Pengfei Xie [1], Tiancheng Pu[1], Gregory Aranovich[1], Jiawei Guo[2], Marc Donohue[1], Ambarish Kulkarni [2 ✉] and Chao Wang [1 ✉]

**Metal-exchanged zeolites have been widely used in industrial catalysis and separation, but fundamental understanding of their structure–property relationships has remained challenging, largely due to the lack of quantitative information concerning the atomic structures and reaction-relevant adsorption properties of the embedded metal active sites. Here, we report on using low-temperature reactive adsorption of NO to titrate copper-exchanged ZSM5 (Cu-ZSM5). Quantitative descriptors of the atomic structures and adsorption properties of Cu-ZSM5 are established by combining atomistic simulation, density functional theory c, operando molecular spectroscopy, chemisorption and titration measurements. These descriptors are then applied to interpret the catalytic performance of Cu-ZSM5 for NO decomposition. Linear correlations are established to bridge low-temperature adsorption analytics and high-temperature reaction kinetics, which are demonstrated to be generally applicable for understanding the structure–property relationships of metal-exchanged zeolites and foregrounded the development of advanced catalytic materials.**

P ortraiture of active sites and their adsorption properties represents a grand challenge but the utmost task for the development of advanced catalysts. Conventionally, it largely relies on microscopic and spectroscopic techniques to characterize the structures of catalytic materials and probe reaction-relevant adsorbates, respectively[1]. However, these approaches are either limited by their insensitivity to the active sites on catalyst surfaces (for example, transmission electron microscopy[1] and X-ray absorption spectroscopy (XAS)[2]) or subject to low signal-to-noise ratios at elevated reaction temperatures and inadequacy of quantitative information (for example, infrared[3] and Raman[4] spectroscopy). In contrast, computational approaches such as density functional theory (DFT) calculations are extensively used to simulate reaction pathways and understand catalytic mechanisms, with the energetics of adsorbing intermediates commonly established as descriptors to understand the trends of kinetic performance and guide catalyst designs[5]. However, such calculations usually require pre-established structure models of catalytic materials, and quantitative validation of the computed structure–property relationships is nontrivial in experiments.

Direct decomposition of NO to $N_2$ and $O_2$ is the most robust strategy for NO removal from combustion emissions as it does not rely on the presence or addition of reductants in the exhaust stream[6]. Cu-ZSM5 represents a promising and extensively studied catalyst for this reaction. Both isolated monomeric[7] and associated dimeric[8,9] Cu sites have been discussed as the active sites. The Cu dimers in Cu-ZSM5 have been probed using various spectroscopic techniques, including ultraviolet–visible spectroscopy[10], Fourier-transform infrared spectroscopy (FTIR)[10], resonance Raman spectroscopy (Raman)[11], electron paramagnetic resonance (EPR)[12] and XAS[13]. Computational studies also support the formation of dicopper-oxo centres ([Cu–O–Cu]$^{2+}$) when $NO_x$ (NO[14,15] or $N_2O$[16]) interacts with Cu-ZSM5. Albeit the abundant evidence for their formation and involvement in the NO decomposition reaction, quantitative characterization

of the Cu dimer motifs remains largely challenging. The overall low population and small coordination number (up to CN = 1) of the Cu sites cause large uncertainties in the assignment of the second-shell feature in extended X-ray absorption fine-structure spectra (EXAFS)[13]. Temperature-programmed reaction (TPR) measurements have been reported to quantify Cu dimers in oxygen-pretreated Cu-ZSM5 of a fixed Si/Al ratio with different Cu exchange levels, but it remains elusive whether this means is generally applicable[17]. Such measurements are also limited due to the inability of obtaining reaction-relevant structure information and adsorption properties, due to the different chemical conditions (for example, $O_2$ versus $NO_x$) in the catalytic process. Similar challenges are also present for other metal-exchanged zeolites that are of broad interest in catalysis and separation[18].

Here, we report the use of reactive adsorption to titrate the atomic structures and elucidate the adsorption properties of metal-exchanged zeolites. On the basis of a series of Cu-ZSM5 zeolites with different Si/Al ratios but all at full exchange, we first performed atomistic simulations to quantify the Cu dimers within the pentasil framework, and conducted TPR measurements to validate the predicted descriptor. We then combined DFT calculations, diffuse reflectance infrared Fourier-transform spectroscopy (DRIFTS) and chromatographic titration of gaseous effluents to evaluate the low-temperature interaction of NO with the series of Cu-ZSM5 zeolites. Reaction-relevant adsorption analytics were derived to establish correlations between the atomic structures and adsorption properties of the Cu sites, which were then employed to interpret the kinetics of NO decomposition catalysed by Cu-ZSM5. We further generalized these relationships to understand the structure–performance correlations for other types of zeolite in NO decomposition and also for Cu-ZSM5 in catalysing methane-to-methanol (MTM) conversion. The aim of our work is to establish the bridge between low-temperature adsorption analytics and high-temperature reaction kinetics in heterogeneous catalysis.

[1]Department of Chemical and Biomolecular Engineering, Johns Hopkins University, Baltimore, MD, USA. [2]Department of Chemical Engineering, University of California, Davis, Davis, CA, USA. ✉e-mail: arkulkarni@ucdavis.edu; chaowang@jhu.edu
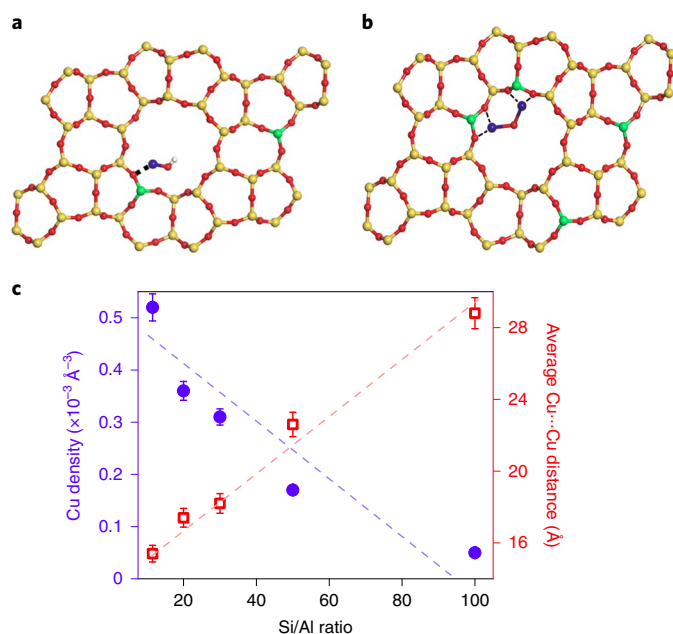
**Table 1 | List of Cu-ZSM5 zeolites with different Si/Al ratios**

| Si/Al | Cu/Al | Surface area (m²g⁻¹) | Cu loading (μmol g⁻¹) | Cu site density (×10⁻³ Å⁻³) | Mean Cu···Cu distance (Å) |
|---|---|---|---|---|---|
| 11.5 | 0.51 | 373 | 487.8 | 0.52 | 15.4 |
| 20 | 0.51 | 373 | 336.74 | 0.36 | 17.4 |
| 30 | 0.48 | 406 | 292.68 | 0.31 | 18.2 |
| 50 | 0.49 | 385 | 154.21 | 0.17 | 22.6 |
| 100 | 0.47 | 396 | 74.59 | 0.08 | 28.8 |



**Fig. 1 | Graphical illustration and characterization of Cu sites in Cu-ZSM5 zeolites. a,b,** Geometric models of a Cu monomer (**a**) and an oxygen-bridged Cu dimer (**b**). Red, oxygen; yellow, silicon; green, aluminum; blue, copper; grey, hydrogen. **c,** Dependences of Cu density (per unit volume of the zeolite pore) and average Cu–Cu distance on the Si/Al ratio. The error bars indicate the s.d. derived from three independent experimental measurements.

## Results

**Synthesis of Cu-ZSM5.** First, we prepared a series of pristine ZSM5 zeolites with different Si/Al ratios (11.5, 20, 30, 50 and 100, as determined by X-ray fluorescence spectroscopy) using hydrothermal synthesis[19]. The as-synthesized ZSM5 molecules exhibited a rectangular parallelepiped shape with an overall particle size in the micrometre scale (Supplementary Fig. 1). They were converted into Na-type zeolites and then Na⁺ was substituted with Cu²⁺ via ion exchange (see Methods)[20]. A Cu/Al ratio of ~0.5 was targeted for full exchange (Table 1). In the following discussion, the Cu-exchanged zeolites are denoted as Cu-ZSM5-$x$, where $x$ represents the Si/Al element ratio (for example, Cu-ZSM5-11.5 represents Cu-ZSM5 with an Si/Al ratio of ~11.5). Brunauer–Emmett–Teller (BET) measurements showed that the five types of Cu-ZSM5 have rather consistent specific surface areas in the range 370−400 m²g⁻¹ (Table 1; see also Supplementary Fig. 2 for the N₂ adsorption and desorption isotherms)[19]. X-ray diffraction patterns collected on the Cu-ZSM5 zeolites exhibited peaks corresponding to the modernite framework inverted (MFI) phase (Joint Committee on Powder Diffraction Standards, JCPDS number 37-0359) but not for copper oxides (Cu₂O or CuO), indicating that the Cu species were highly dispersed in the zeolites (Supplementary Fig. 3).

To study the interaction with NO, the Cu-ZSM5 zeolites were pretreated in He at 500 °C. After activation, the Cu species in Cu-ZSM5 can be present either as monomers ([Cu⁺]) or in a dimeric configuration [Cu⁺···Cu⁺] via an auto-reduction process[13,15,21,22], with the charges balanced by one or two proximal Al centres in the framework, respectively (Fig. 1a,b)[21]. This was confirmed using DRIFTS analysis to track the hydroxyl (O–H) and framework features during the pretreatment in He (Supplementary Fig. 4). It has been suggested that the Cu dimers are accommodated within the ten-membered ring of ZSM5 and associated with two Al sites separated by one (1T) or two (2T) SiO₄ tetrahedra units, following Löwenstein's rule[23]. The Cu density in the five types of Cu-ZSM5 zeolite varied with the Si/Al ratio, decreasing from 0.52×10⁻³ Å⁻³ for Cu-ZSM5-11.5 to 0.08×10⁻³ Å⁻³ for Cu-ZSM5-100 (Table 1 and Fig. 1c). These values correspond to a nearly linear increase in the average distance between neighbouring Cu sites from 15.4 to 28.8 Å. Note that the Cu density here refers to the average number of Cu sites per unit volume of the zeolite pore, with the latter determined by BET measurements (Table 1 and Supplementary Fig. 2). The average Cu···Cu distance was determined from the Cu density by assuming a cubic occupation of the Cu atoms within the unit pore volume, which is different from the actual distance between neighbouring Cu sites, as to be discussed below[24]. Previously, Schoonheydt and Solomon et al.[11,13,16] have used XAS, ultraviolet–visible spectroscopy, Raman and DFT to determine the geometry of dimeric Cu motifs in Cu-ZSM5, showing Cu···Cu distances of 2.5–4.2 Å and a bond angle of ~140° for Cu−O−Cu. Nonetheless, it remains challenging to quantify the atomic fractions of Cu dimers

($\eta_{Cu···Cu}$; namely, the percentage of Cu atoms being in dimeric configuration) within Cu-ZSM5 and to characterize their adsorption properties using these methods.

The five types of Cu-ZSM5 form a platform with a consistent framework but varying atomic structures of Cu sites. Upon interaction with NO, Cu⁺ can be oxidized to Cu²⁺, which is associated with structural transformation of the Cu sites (for example, the formation of oxo-Cu centres) and adsorption of nitrogen oxide species. Analysis of these adsorbates thus provides a viable approach towards quantitative titration of $\eta_{Cu···Cu}$ and adsorption properties for the metal-exchanged zeolites.

**Fractions of Cu dimers within Cu-ZSM5.** To quantify the fraction of Cu-dimer species within the Cu-ZSM5 zeolites of various Si/Al ratios, we first performed high-throughput periodic DFT calculations (Perdew–Burke–Ernzerhof functional; Grimme D3(BJ) van der Waals corrections; 500 eV plane-wave cut-off; Γ point only; implemented in the Vienna Ab-initio Simulation Package) to evaluate the formation energy of all distinct [Cu–O–Cu]²⁺ dimer configurations for the MFI topology. Specifically, for each inequivalent T site position of Al (12 total unique T sites for MFI; Supplementary Tables 1 and 2), we systematically replaced every T atom with Al within a threshold distance of 9.0 Å, resulting in a database of 167 structures (Si/Al = 47; 115 unique configurations). For each of these structures, we calculated dimer formation energies using:

$$Z'Cu + Z''Cu + 0.5\,O_2 \rightarrow Z'[Cu-O-Cu]Z'' + Z_{Si} \qquad (1)$$

where Z′ and Z″ represent one Al substitution in the MFI framework and $Z_{Si}$ represents the energy of an all-silica MFI framework. Although direct comparison of various Z′[Cu–O–Cu]Z″ configurations is possible (Supplementary Fig. 5), equation (1) allows for separate analysis of the stability of [Cu–O–Cu]²⁺ motifs (which depends on reaction conditions and the oxygen chemical potential)
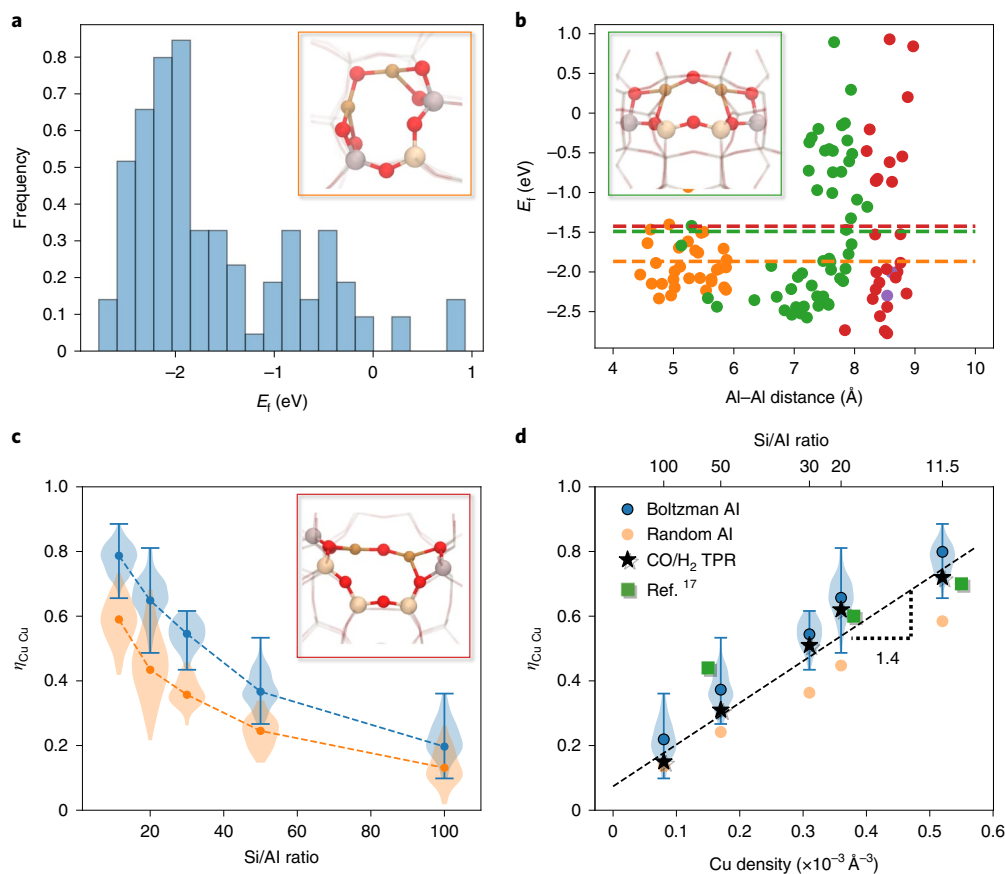
**Fig. 2 | DFT-calculated Cu dimer fractions in Cu-ZSM5. a**, Histogram showing the distribution of dimer formation energies ($E_f$) for all possible [Cu–O–Cu]$^{2+}$ dimers in MFI. **b**, $E_f$ values at different Al–Al distances with various numbers of Si atoms between the two Al sites (orange = 1T; green = 2T; red = 3T; purple = 4T). The dotted lines show the average $E_f$. **c**, Cu dimer fractions in MFI ($\eta_{Cu\cdots Cu}$) at 80 °C assuming a Boltzmann-weighted (blue) or a random (orange) distribution of Al sites. **d**, Linear relationship between the Cu dimer fraction, as derived from DFT calculations (blue) and TPR measurements (black stars) and the Cu density and Si/Al ratio. The experimental data from ref. [17] (green squares) are shown to be consistent with our evaluations. The insets in **a**,**b** and **c** show the structures of the most favourable 1T, 2T and 3T dimer configurations, respectively. The error bars in **c** and **d** indicate the statistical distribution of the computed Cu dimer fractions.

and the underlying Al distribution (which probably depends on the synthesis conditions). The choice of the $O_2$ gas-phase reference was motivated by previous work[25,26]. Fig. 2a summarizes the distribution of calculated dimer formation energies, with the wide span (>2.5 eV) probably due to the favourable formation of dimers from certain Al pairs. Moreover, Fig. 2b shows that, although dimers accommodated by the Al pairs separated with one (orange) silicon atom are on average more favourable (dotted lines; Fig. 2b), certain configurations (see insets in Fig. 2b) separated with two (green) or three Si atoms (red) are also very stable. The formation energies are summarized in Supplementary Tables 1 and 2 and the optimized periodic structures are provided in Supplementary Data 1 as an Atomic Simulation Environment database file[27].

As the fraction of dimers formed for a given Si/Al ratio depends on the proximity and distribution of Al atoms, we used Monte Carlo simulations to create ensembles of structures corresponding to various Si/Al ratios to obtain a statistical sampling of the relative Al locations. Considering the Al siting in MFI depends on the synthesis conditions and is still widely debated[28], we chose to determine the Al distribution using DFT. Specifically, two extremes are shown in Fig. 2c: (1) the Al distribution is completely determined by DFT-calculated thermodynamics of Al substitution (that is, Boltzmann weighted); and (2) thermodynamics are not relevant and Al distributes randomly. In conjunction with the dimer formation energies in Fig. 2b, and after incorporation of

entropic effects, these ensembles of Al distributions were used to estimate $\eta_{Cu\cdots Cu}$ for each Si/Al ratio at 80 °C (the temperature used in our titration experiments; see Methods). Realizing that some Al atoms are capable of stabilizing [Cu–O–Cu]$^{2+}$ dimers with multiple other Al atoms (especially at low Si/Al ratios), we populated the Al sites by starting with the most favourable [Cu–O–Cu]$^{2+}$ dimer configurations. Once an Al pair was assigned with a Cu dimer, the two Al atoms were excluded from further assignment of less stable dimers. Using this approach, the value of $\eta_{Cu\cdots Cu}$ predicted according to the Boltzmann-weighted distribution varied from 0.79 for Cu-ZSM5-11.5 to 0.20 for Cu-ZSM5-100. In general, the Boltzmann-weighted distribution of Al atoms gave an approximately 20–30% higher $\eta_{Cu\cdots Cu}$ than the random Al distribution. More broadly, the calculated $\eta_{Cu\cdots Cu}$ based on both Boltzmann and random distributions exhibited nearly linear dependence on the average Cu site density (Fig. 2d). This correlation confirms that our simulation captures the higher tendency of forming Cu dimers for lower Si/Al ratios due to the closer proximity of Al atoms. As is also shown in Fig. 2c,d, $\eta_{Cu\cdots Cu}$ exhibits a nonlinear dependence on the Si/Al ratio. The results for other temperatures (Supplementary Fig. 6) indicated that, although the fraction of dimers reduced slightly at higher temperatures, the overall trends remained the same, as the [Cu–O–Cu]$^{2+}$ dimer can be stabilized by multiple types of Al pairs. This suggests that the MFI topology is favourable for the formation of dimers and, as we show later,

low-temperature adsorption measurements can be used to probe the active sites relevant to high-temperature reactivities.
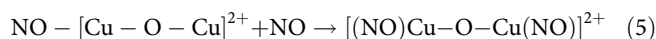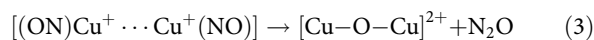
Although Cu-ZSM5 has been extensively studied, only a few reports are present for experimental quantification of the Cu dimer fractions. Iglesia et al.[17] used CO/H$_2$ TPR to evaluate $\eta_{Cu\cdots Cu}$ in Cu-ZSM5 with Si/Al = ~13–14 and Cu/Al = ~0.12–0.6 and derived $\eta_{Cu\cdots Cu}$ = ~44, 60 and 70% for Cu-ZSM5 with Cu/Al = 0.12, 0.38 and 0.58, respectively. Owing to the limited follow-up studies using this method, its general applicability is still to be demonstrated. Moreover, CO/H$_2$ temperature-programmed reduction (TPR) cannot provide information about the atomic structures and adsorption properties that are pertinent to the catalytic applications (for example, in the presence of *NO$_x$ for NO decomposition and selective catalytic reduction). Moretti et al.[15] combined irreversible CO adsorption at 298 K and N$_2$ adsorption at 273 K to evaluate the abundance of Cu dimers in Cu-ZSM5 by assuming strong and selective adsorption of N$_2$ on Cu dimers. However, this method was later on questioned by Itadani et al.[29], who studied N$_2$ adsorption on Cu-MFI using a series of spectroscopic methods, including photoluminescence, X-ray absorption and infrared, and concluded that there is selective adsorption of N$_2$ on monomeric Cu$^+$, rather than Cu dimers. Henriques et al.[30]. attempted to use electron paramagnetic resonance measurements to obtain quasi-quantitative information for the atomic structures of Cu sites within Cu-ZSM5, but debates are present on the corresponding peak assignments. We performed CO/H$_2$ TPR measurements on the series of Cu-ZSM5-$x$ zeolites with pretreatment in oxygen (that is, 500 °C for ~2 h, to induce the formation of [Cu–O–Cu]$^{2+}$ centres) (Supplementary Fig. 7 and Supplementary Table 3). Figure 2d summarizes the data collected from both the literature[17] and our own CO/H$_2$ TPR measurements with similar pretreatments. The results largely resemble the linear relationship correlating $\eta_{Cu\cdots Cu}$, calculated based on the Boltzmann distribution and dimer formation via equation (1), with the average Cu site density. The fact that our predictions are in close agreement with these experiments not only validates the predicted distribution and structures of Cu sites, but also suggests that the established linear scaling relationship is intrinsic to the zeolite-supported metal sites. The initial Boltzmann Al distributions are obtained using only the energetics of substituting a single Si atom with a single Al (with the most favourable Brønsted H location; Supplementary Table 1). While the existing Al atoms may influence the siting of the other Al, such analyses are beyond the scope of this work. While not discussed here, we note that the above Monte Carlo approach can be extended based on the experimentally determined Al positions that are influenced by kinetic factors. Moreover, we acknowledge that migration of Al sites is also possible during oxidative pretreatment and the process of Cu dimer formation[31].

**Reactive adsorption of NO on Cu-ZSM5.** As noted, $\eta_{Cu\cdots Cu}$ evaluated using CO/H$_2$ TPR cannot be directly related to the active sites involved in the NO decomposition reaction. This is due to the dissimilar formation energies of dicopper-oxo centres upon exposure to different oxidants (for example, O$_2$, H$_2$O$_2$ and N$_2$O)[19,28,32]. To merge this gap, we turned to evaluate the reactive adsorption of NO on Cu-ZSM5, aiming to probe the structure and property of the Cu sites under reaction-relevant environments. We also started with calculations of free energies for the various nitrogenous adsorbates and reaction barriers possibly involved in the interaction between NO and the Cu sites using the nudged elastic band and dimer methods (Supplementary Fig. 8). Consistent with the previously reported approaches[14,33], the simulation was primarily applied to 1T and 2T site models of Cu dimers (Fig. 3a; for comparison, Fig. 3b shows the scenery on Cu monomers). A more extensive analysis applying the ensemble average to the comprehensive set of data presented in Fig. 2 is currently underway and will be reported in a separate study.

NO decomposition on the [Cu$^+$···Cu$^+$] dimer sites involves three barriers related to: (1) bending of the NO molecule (TS1); (2) cleaving of the first N–O bond to form the [Cu–O–Cu]$^{2+}$ dimer (TS2); and (3) reaction of N$_2$O with the [Cu–O–Cu]$^{2+}$ dimer for O$_2$ formation (TS3), where the barrier TS3 (1.6 eV; Fig. 3c,d) is probably inaccessible at 80 °C (rate = ~10$^{-10}$ s$^{-1}$). Moreover, the single NO-bound state NO–[Cu–O–Cu]$^{2+}$ (Fig. 3e) is predicted to be most favourable at relatively low temperatures (for example, below 100 °C), although binding of N$_2$O (black) or a second NO (Fig. 3f) is within 0.2 eV. Finally, the reaction of desorbed N$_2$O with a second [Cu$^+$···Cu$^+$] site is favourable and results in the formation of N$_2$ (Supplementary Figs. 9–11). NO decomposition on the Cu$^+$ monomer is also investigated in Fig. 3f.

To validate the predicted reaction pathway, we used DRIFTS to characterize the stable adsorbates formed on Cu-ZSM5 upon interaction with gasous NO (NO(g)). Figure 4a presents the time-dependent spectra collected on Cu-ZSM5-11.5 under a flow of 1,500 ppm NO at 80 °C (see the temporal profiles for the other four zeolites in Supplementary Fig. 12). Figure 4b,c shows comparisons of the spectra recorded on Cu-ZSM5-11.5 with different partial pressures of NO ($p_{NO}$) and on different Cu-ZSM5 zeolites with 1,500 ppm NO, respectively (all at 15 min; see Supplementary Figs. 13 and 14 for more details). The corresponding peak assignments are summarized in Supplementary Table 4.

The spectra recorded on Cu-ZSM5-11.5 featured two peaks located at 1,903 and 1,813 cm$^{-1}$. The intensities of these two peaks exhibited an inverse relationship with the time elapsed during NO adsorption before saturation was reached at ~15 min (Fig. 4d and Supplementary Fig. 15). As reported by Beutel et al.[22], this behaviour can be attributed to the oxidation of Cu$^+$ and the formation of dicopper-oxo centres via the following reactions, rationalized by the measured slope of −1, assuming that extinction coefficients of NO on Cu$^+$ and Cu$^{2+}$ are similar:

$$[Cu^+ \cdots Cu^+] + 2NO \rightarrow [(ON)Cu^+ \cdots Cu^+(NO)] \qquad (2)$$

$$[(ON)Cu^+ \cdots Cu^+(NO)] \rightarrow [Cu-O-Cu]^{2+} + N_2O \qquad (3)$$

$$[Cu-O-Cu]^{2+} + NO \rightarrow NO-[Cu-O-Cu]^{2+} \qquad (4)$$

$$NO-[Cu-O-Cu]^{2+} + NO \rightarrow [(NO)Cu-O-Cu(NO)]^{2+} \qquad (5)$$

where the transition from the 1,813 cm$^{-1}$ peak to the 1,903 cm$^{-1}$ peak indicates the conversion of [(ON)Cu$^+$···Cu$^+$(NO)] to one or two NO molecules bound to [Cu–O–Cu]$^{2+}$. Our assignment was further corroborated by the DRIFTS spectra collected at saturation (15 min) under $p_{NO}$ (Fig. 4b). As $p_{NO}$ was increased from 300 to 1,500 ppm, the intensity of the 1,813 cm$^{-1}$ peak decreased, whereas that for the 1,903 cm$^{-1}$ peak increased (Supplementary Fig. 16). Similar to the temporal response, this transition with $p_{NO}$ was also associated with the transformation from [(ON)Cu$^+$···Cu$^+$(NO)] to NO–[Cu–O–Cu]$^{2+}$ (including both one and two NO molecules per Cu dimer site; [(NO)Cu–O–Cu]$^{2+}$ and [(NO)Cu–O–Cu(NO)]$^{2+}$, respectively) as a result of the equilibrium shift of reactions shown in equations (2)–(5) towards the right-hand sides at increasing concentrations of NO. These assignments were consistent with DFT-predicted stable adsorbates involved in the low-temperature interactions and trends of vibrational frequencies (for example, for 1T Cu dimer models, NO–[Cu–O–Cu]$^{2+}$ (1,871 cm$^{-1}$) = ~[(ON)Cu–O–Cu(NO)]$^{2+}$ (1,913 cm$^{-1}$) and [(ON)Cu$^+$···Cu$^+$(NO)] (1,796 cm$^{-1}$); Supplementary Fig. 17). Although different dimer configurations may result in small variations in the predicted vibrational frequencies, performing these calculations for all 115 unique
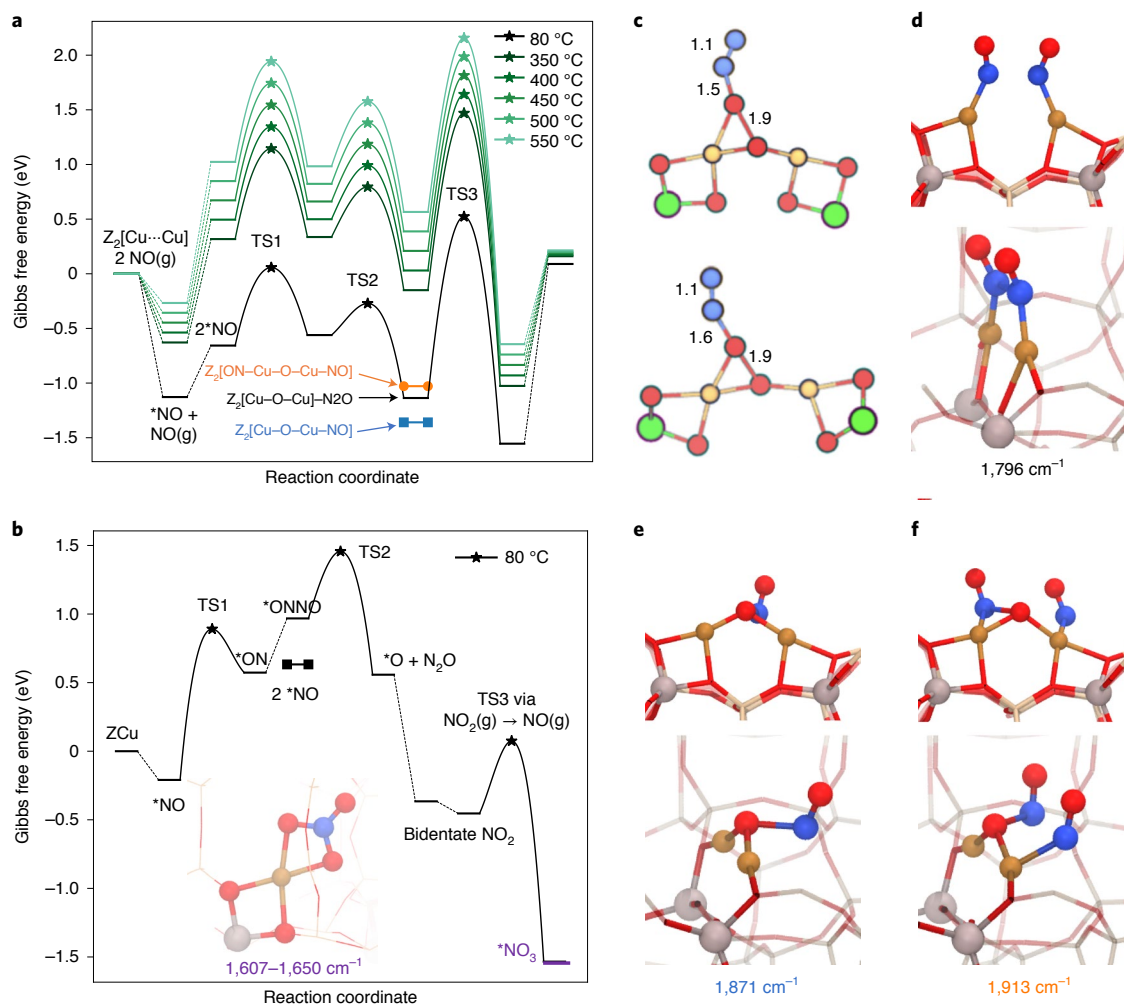
**Fig. 3 | DFT-calculated pathways for the reactive adsorption of NO on Cu-ZSM5. a**, DFT-calculated free-energy diagrams at various temperatures for NO decomposition by on the Cu dimer in 1T configuration. The free energies of one and two NO-bound dimers are shown in orange and blue, respectively. **b**, The scenery on Cu monomers at 80 °C. The inset shows the DFT-optimized $[Cu-NO_3]^+$ structure and the predicted vibrational frequency. **c**, Transition states for $N_2O$ decomposition on 1T (top) and 2T (bottom) models of Cu dimers (red, O; blue, N; yellow, Cu; green, Al). **d-f**, Front (top) and side (bottom) views of DFT-optimized structures for (**d**) $[(ON)Cu^+\cdots Cu^+(NO)]$, (**e**) $NO-[Cu-O-Cu]^{2+}$ and (**f**) $[(NO)Cu-O-Cu(NO)]^{2+}$ (red, O; blue, N; yellow, Cu; grey, Al).

positions in MFI is beyond the scope of this work; no significant changes are expected though.

Besides the two primary peaks, minor features were also present at 2,156 and 1,653 cm⁻¹, both of which exhibited a monotonic increase in intensity with time. The peak at 2,156 cm⁻¹ can be assigned to $NO^+$ associated with the Brønsted acid sites[34]. The 1,653 cm⁻¹ peak was not commonly observed in the previous spectroscopic studies of nitrogenous adsorbates on Cu-ZSM5. It could be associated with the asymmetric stretching vibration of the $-NO_2$ moiety in dinitrogen trioxide species (for example, $Cu^+-O_2N=NO$, with reported peak positions at 1,644–1,653 cm⁻¹)[35], which has previously been suggested as a critical intermediate for partial reduction of NO to $N_2O$ on Cu monomers. However, this peak exhibited a clear downshift as the Si/Al ratio increased, reaching 1,636 cm⁻¹ for Cu-ZSM5-100 (Fig. 4c), where most of the copper species are probably in the monomeric configuration (~80%; Fig. 2d).

Motivated by this observation, we used DFT calculations to study the reaction mechanism on isolated Cu cations in ZSM5 (refs. [36,37]). As summarized in Fig. 3b, we concluded that the reaction mechanism proceeds through three transition states: TS1 (rotation of *NO to form *ON); TS2 (breaking of *ONNO to from bound

*O and $N_2O$); and TS3 (reaction of bidentate $NO_2$ to form $*NO_3$). Our results show that adsorbed $*NO_3$ (denoted as $ZCu-NO_3$) represents the most stable state of isolated Cu monomers at low temperatures as the barriers for reactions with $NO_2$ (to form NO; 1.6 eV) and $N_2O$ (to form NO; 2.4 eV) are probably insurmountable at 80 °C. To further confirm the presence of $ZCu-NO_3$ for unpaired Al sites, we calculated the vibrational frequencies for all 12 unique T sites using DFT. As summarized in Supplementary Table 5 and also shown as an insert in Fig. 3d, the DFT-predicted frequencies (1,607–1,650 cm⁻¹) were in very good agreement with experimental measurements (1,636 cm⁻¹). Based on the above experimental observations and computational predictions, the interaction of Cu monomers with NO can be summarized as:

$$Cu^+ + 2NO + NO_2 \rightarrow Cu - NO_3 + N_2O \qquad (6)$$
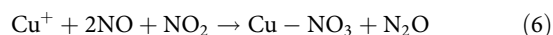
After assigning the spectroscopic features, we could now compare the spectra of the five types of Cu-ZSM5 with different Si/Al ratios. As shown in Fig. 4c, the intensities of all of the features reduced as the Si/Al ratio increased, as expected with the smaller Cu (or Al) site density in the zeolites. Interestingly, the relative
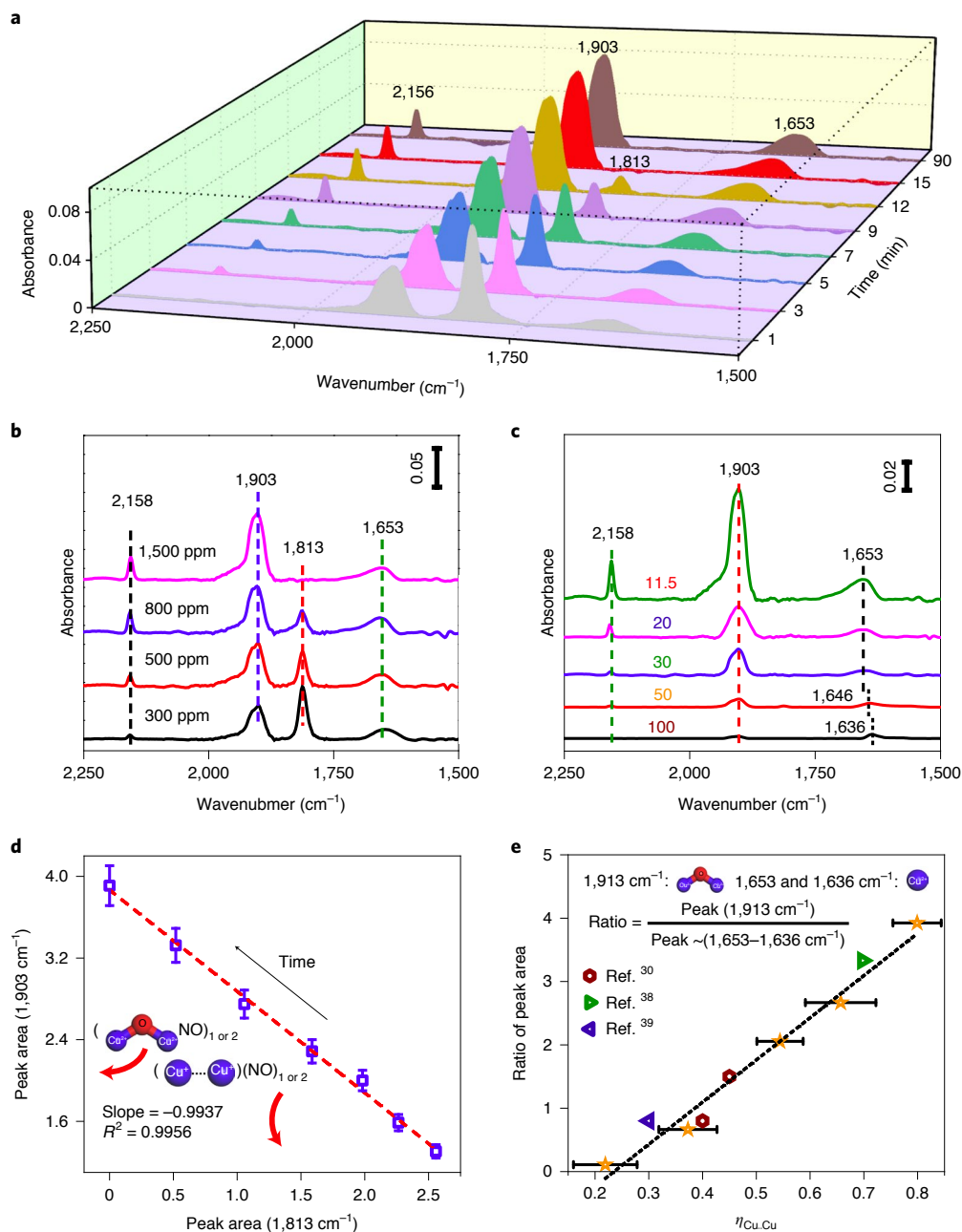
**Fig. 4 | Characterization and quantification of Cu dimers in Cu-ZSM5 zeolites. a**, Time-dependent DRIFTS analysis of NO (1,500 ppm) adsorption on Cu-ZSM5-11.5 at 80 °C. **b**, Pressure-dependent DRIFTS analysis of NO adsorption at 80 °C on Cu-ZSM5-11.5 at 15 min. **c**, DRIFTS analysis of NO adsorption at 80 °C on Cu-ZSM5 with different Si/Al ratios at 1,500 ppm and 15 min. **d**, Correlation of integrated peak areas of the 1,903 cm$^{-1}$ peak and 1,813 cm$^{-1}$ peak in DRIFT spectra of NO adsorption at 80 °C and 1,500 ppm on Cu-ZSM5-11.5 at different times. The error bars indicate the s.d. of peak area integration derived from three independent experimental measurements. **e**, Correlation of area ratios of the 1,903 cm$^{-1}$ peak and 1,813 cm$^{-1}$ peak in DRIFT spectra of NO isothermal adsorption at 80 °C on Cu-ZSM5 and Cu dimer fraction from DFT calculation. The error bars represent the statistical distribution of the computationally simulated Cu dimer fractions.

intensities of the two peaks at 1,903 and 1,653–1,636 cm$^{-1}$ exhibited opposite trends. Specifically, the peak area ratio (1,903 versus 1,653–1,636 cm$^{-1}$) observed from DRIFTS scaled well with $\eta_{Cu\cdots Cu}$ as derived from atomistic simulation and TPR measurements, with the slope determined to be 6.66 (Fig. 4e). As we discussed above, the two DRIFTS peaks were assigned to adsorbates associated with Cu dimers and monomers, which was also consistent with the relatively high stabilities of the $[(NO)Cu-O-Cu]^{2+}$ (or $[(NO)Cu-O-Cu(NO)]^{2+}$) and $[Cu-NO_3]^+$ motifs associated with the corresponding Cu sites, as

suggested by DFT calculations (Fig. 3a and Supplementary Fig. 17). We further compared the previously reported DRIFTS data[30,38,39] with our results in Fig. 4e. As $\eta_{Cu\cdots Cu}$ was not resolved in these previous studies, we estimated it using the linear scaling relationship established in Fig. 2d and the reported Cu site densities. It can be seen that these data points also follow well the linear trend established for the Cu-ZSM5 zeolites in this work. The linear relationship shown in Fig. 4e thus not only confirms the more favourable formation of Cu dimers at higher Cu site densities under the reaction-relevant
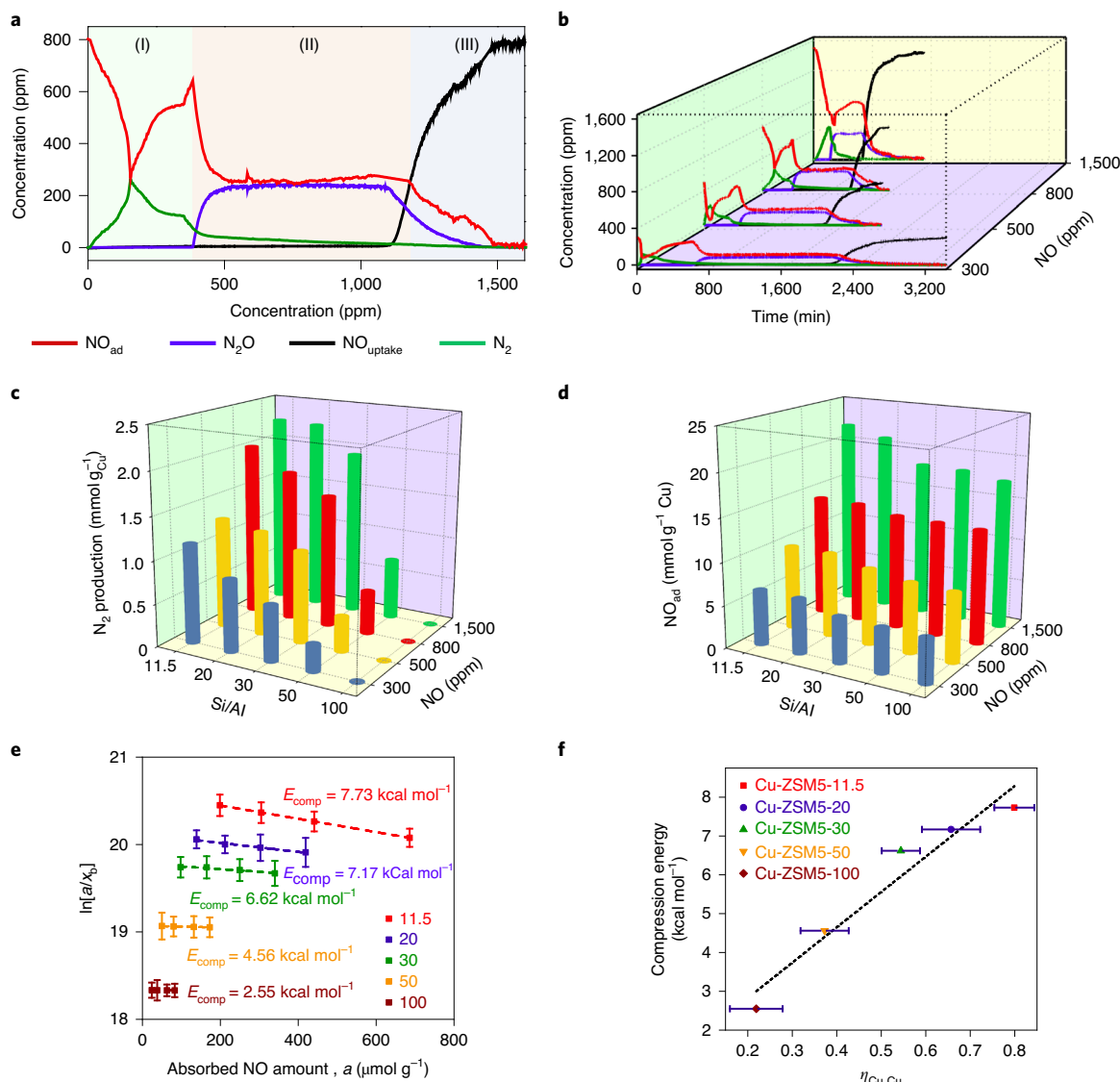
**Fig. 5 | NO isothermal adsorption profiles. a**, Time-dependent profiles of outlet concentrations of NO, $N_2O$ and $N_2$ during NO isothermal adsorptions at 80 °C with 800 ppm NO on Cu-ZSM5-11.5. **b**, Time-dependent profiles of outlet concentrations of NO, $N_2O$ and $N_2$ during NO isothermal adsorptions at 80 °C with different pressures of NO for Cu-ZSM5-11.5. Labels I, II and III represent different stages of the NO adsorption process; further details are provided in the text. **c**, Plot of $N_2$ production per Cu site during NO isothermal adsorption at different NO pressures on the five Cu-ZSM5 zeolites. **d**, Plot of $NO_{ad}$ per Cu site during NO isothermal adsorption at different NO pressures on Cu-ZSM5 zeolites. **e**, Ono–Kondo plots of compression energies of Cu-ZSM5 zeolites. The term $a/x_b$ represents the normalized ratio of adsorption capacity ($a$) to the molecule density in the bulk ($x_b$). The error bars indicate the s.d. of three experimental measurements of $NO_{ad}$ isotherms. **f**, Correlation of compression energy and Cu dimer fraction in Cu-ZSM5 zeolites (fitted equation: $y = 9.1x + 1.0$). The error bars represent the statistical distribution of the computationally simulated Cu dimer fractions. In panels **a** and **b**, red represents $NO_{ad}$, green represents $N_2$ production, blue represents $N_2O$ production and black represents NO uptake.

environment, but also indicates that the quantity of $\eta_{Cu\cdots Cu}$ evaluated from $CO/H_2$ TPR measurements (with oxygen pretreatment, as shown in Fig. 2d) is linearly correlated to the Cu dimer fractions formed upon exposure to $NO_x$. Such a linear relationship thus allows for employment of $\eta_{Cu\cdots Cu}$ to interpret the structures and properties of Cu-ZSM5 under reaction-relevant conditions[15].

**Titration of effluents.** In addition to the spectroscopic analyses, we performed independent measurements of the gaseous effluents during the low-temperature interaction of NO with Cu-ZSM5, to acquire more quantitative information on the adsorption properties. This was done under the same temperature and NO partial pressures (that is, 80 °C and 300–1,500 ppm of NO) using a plug flow reactor instead of the in situ DRIFTS cell (see Methods and

Supplementary Fig. 18). The outlet gas was typically composed of $N_2$ and $N_2O$ produced from the redox interactions between NO and the Cu sites in the zeolites, as well as residual nitric oxide ($NO_{res}$) left in the gas stream (Figs. 5a,b and Supplementary Fig. 19). The rate of NO adsorption ($NO_{ad}$) over the course was determined by calculating the mass balance of nitrogen (see Methods). Quantitative summaries for the different molecule species are provided in Supplementary Tables 6–10. It should be pointed out here that the differences in flow pattern, flow rate and catalyst loading between these two sets of experiments are not expected to alter the chemical nature and fractions of adsorbates over the course of interaction, but only the timescale of the equilibration process.

The effluent profiles featured a long transient period, typically composed of three stages. Using 800 ppm NO on Cu-ZSM5-11.5 as
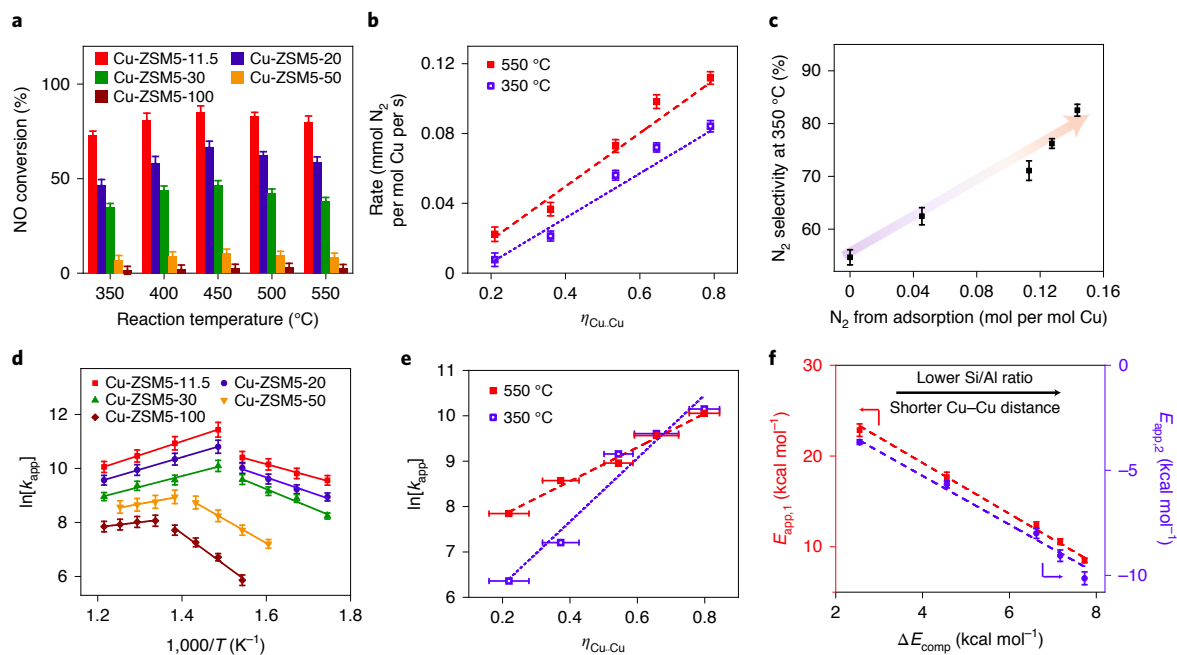
**Fig. 6 | Catalytic performance and kinetics of NO decomposition. a**, Conversion of NO over different Cu-ZSM5 zeolites. **b**, Correlation between the rate of $N_2$ formation at 350 and 550 °C and fractions of Cu dimers. **c**, Correlation of $N_2$ selectivity at 350 °C with $N_2$ production derived from reactive adsorption of NO. **d**, Arrhenius plots for rate constants versus $1/T$. **e**, Correlation between $\ln[k_{app}]$ at 350 and 550 °C and fractions of Cu dimers. **f**, Correlation between apparent activation energies at low (red) and high temperatures (blue) and the compression energy derived from Ono–Kondo analysis. The error bars in **a**–**d** and **f** indicate the s.d. derived from three independent experimental measurements. The error bars in **e** represent the statistical distribution of the computationally simulated Cu dimer fractions.

an example, Fig. 5a shows that during stage I (that is, 0–384 min), only $N_2$ was present in the outlet. The concentration of produced $N_2$ initially increased with time and reached a maximum of 268 ppm, then dropped from the peak value to 73 ppm. Correspondingly, the $NO_{ad}$ profile presented a fast drop from nearly 800 ppm at the beginning to a minimum of 264 ppm, then a rise to a peak value of 643 ppm. The amounts of residual NO ($NO_{res}$) and $N_2O$ detected in the outlet were negligible during this stage. Stage II started with a fast drop of $NO_{ad}$ and an increase in $N_2O$, which then reached a plateau at ~260–270 ppm and ~240 ppm, respectively. During this period, $N_2$ gradually phased out and no $NO_{res}$ was present in the outlet. The last stage (III) was a transition process towards saturation, with both $N_2O$ and $NO_{ad}$ decreasing to zero and $NO_{res}$ restoring to the feeding concentration (800 ppm). Similar behaviours were exhibited in the other adsorption profiles recorded on the different types of zeolite and/or at various concentrations of NO, although there were variations in the lengths and concentrations of nitrogenous species in each stage (Fig. 5b and Supplementary Fig. 19).

The $NO_{ad}$ profiles presented above carry abundant thermodynamic and kinetic information about the redox chemistry between NO and the Cu sites. Without going into the details of the kinetics here, we focus on the cumulative production of $N_2$ and the equilibrium state of $NO_{ad}$ in the present discussion, aiming to assess the atomic structures and adsorption properties of the Cu sites in the zeolites. As previously suggested in Supplementary Fig. 9, the production of $N_2$ from the low-temperature interaction between Cu-ZSM5 and NO can be attributed to the following reaction[40]:

$$[Cu^+ \cdots Cu^+] + N_2O \rightarrow [Cu-O-Cu]^{2+} + N_2 \qquad (7)$$
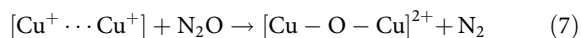
where $N_2O$ can be derived from the reactions in equations (2) and (3). The total amount of $N_2$ detected during the reactive adsorption process increased with $p_{NO}$ as more $N_2O$ was accessible for the reaction

shown in equation (7) (Fig. 5c). A more interesting observation was the production of more $N_2$ for the zeolites with lower Si/Al ratios (Fig. 5c). As indicated by the combination of the reactions shown in equations (3) and (7), the production of one $N_2$ molecule involved two Cu dimers. Cu monomers were associated with the reaction shown in equation (6) and would not contribute to the production of $N_2$ at the relatively low temperature (80 °C) employed here. Therefore, the amount of $N_2$ produced from the $NO_{ad}$ process was also quantitatively indicative of the abundance of Cu dimers in the zeolites. The correlation between $N_2$ evolution and $\eta_{Cu \cdots Cu}$ exhibited a two-stage behaviour (Supplementary Fig. 20). Fundamental understanding of these behaviours was obscured by the interweaving and competitive kinetics of the reactions shown in equations (6) and (7) during the interaction between Cu-ZSM5 and NO, but the more favourable production of $N_2$ at a higher abundance of Cu dimers was obviously an outcome of the higher probability of an $N_2O$ molecule generated from the reaction shown in equation (3) (or from Cu monomers in the process of forming $[Cu-NO_3]^{2+}$, equation (6)) encountering another Cu dimer and being further reduced to $N_2$ via the reaction shown in equation (7). It is conceivable that this probability became less sensitive to the increase in $\eta_{Cu \cdots Cu}$ at a high abundance of Cu sites, given the expectation that it approached saturation when $\eta_{Cu \cdots Cu}$ became close to 1.

The specific capacity of $NO_{ad}$ was found to be insensitive to the Si/Al ratio but sensitive to $p_{NO}$ (Fig. 5d). For example, the specific capacity was consistently at ~2.03 mmol g$^{-1}$ Cu for the five types of zeolite under 800 ppm NO. Quantitative analysis of the $NO_{ad}$ capacities was performed in the framework of Ono–Kondo coordinates (see Methods) to derive the adsorption energy ($\Delta E_{NO}$) and compression energy ($\Delta E_{comp}$)[41]. The latter term ($\Delta E_{comp}$) describes the interaction between adjacent adsorbates[42]. In the case of $NO_{ad}$ on Cu-ZSM5, $\Delta E_{comp}$ is indicative of the apparent difference in free energy between $[Cu-O-Cu(NO)]^{2+}$ and $[(NO)Cu-O-Cu(NO)]^{2+}$; namely, the
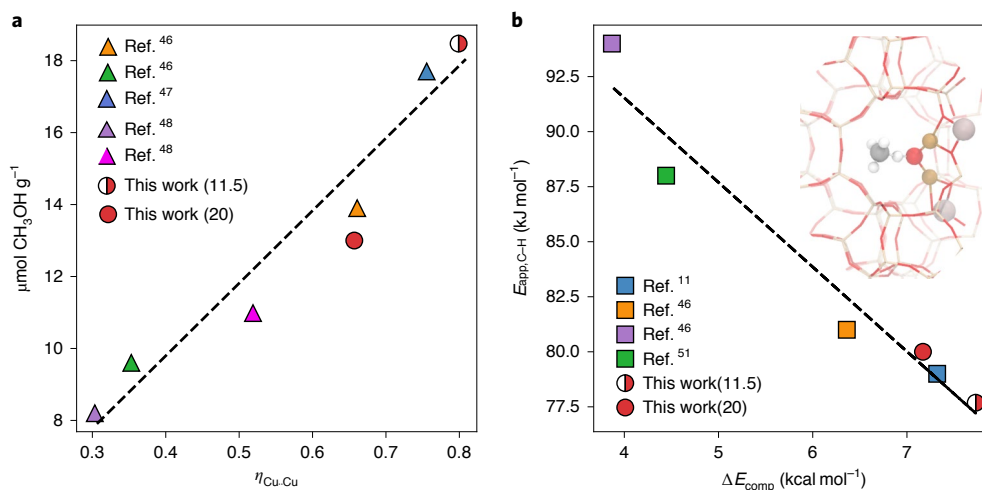
**Fig. 7 | Catalytic study of MTM using Cu-ZSM5 from the literature and this work. a**, Correlations between methanol yields and Cu dimer fractions.
**b**, Correlation between apparent methane activation energies and compression energies; the inset structure shows the adsorption of $CH_4$ on Cu-ZSM5. Here, the Cu dimer fractions and compression energies were derived by fitting the Cu densities from the literature into the scaling established in Figs. 2d and 5f.

dimeric Cu motifs with one or two NO adsorbates. Figure 5e shows the $p_{NO}$-dependent adsorption capacities plotted in the generalized Ono–Kondo coordinates for the five types of zeolite (at 80 °C). $\Delta E_{NO}$ derived from the intercepts was determined to be ~33.5 kcal mol$^{-1}$ for Cu-ZSM5, which matches well with the calculated value of ~1.4 eV (32.2 kcal mol$^{-1}$) for [Cu–O–Cu(NO)]$^{2+}$. The negative slopes indicate positive $\Delta E_{comp}$. The derived $\Delta E_{comp}$ was dependent on the Si/Al ratio and, correspondingly, $\eta_{Cu\cdots Cu}$, which varied from 2.55 kcal mol$^{-1}$ for Cu-ZSM5-100 to 7.73 kcal mol$^{-1}$ for Cu-ZSM5-11.5.

As $\Delta E_{comp}$ derived from the NO$_{ad}$ isotherms represents a statistical average of all Cu sites and no competitive adsorption of NO is expected on monomeric Cu sites (which are occupied by nitrate adsorbates; equation (6)), we expected that the Cu-ZSM5 with more abundant Cu dimers would be more subject to adsorption compression. This inference was confirmed with the positive and linear correlation between $\Delta E_{comp}$ and $\eta_{Cu\cdots Cu}$, as shown in Fig. 5f. Noticeably, the calculated difference in free energy between [(NO)Cu–O–Cu]$^{2+}$ and [(NO)Cu–O–Cu(NO)]$^{2+}$ was ~0.3 eV, which corresponds well to the maximum value of $\Delta E_{comp}$ (~7–8 kcal mol$^{-1}$) observed from the Ono–Kondo analysis of the NO$_{ad}$ capacities, and confirms the compression energy measurement as a viable means to evaluate the adsorption properties of the Cu sites within Cu-ZSM5. Thereby, $\Delta E_{comp}$ is a measurable descriptor of the adsorption properties for the Cu sites. Furthermore, a close view of their relationship finds slight deviation from the linear fitting, with $\Delta E_{comp}$ levelling off at high Cu dimer fractions. Such deviation indicates the presence of secondary effects, in addition to the population of dimers, contributing to the adsorption compression. It is likely that the Cu$\cdots$Cu distance[13,15,24,43] and Cu–O–Cu bonding angle[11,16] have weak dependence on the Si/Al ratio, probably originating from the Boltzmann (instead of completely random) distribution of Al sites, which has led to somewhat more favourable exposure of certain Cu dimer configurations (Supplementary Table 2)[14,44] at low Si/Al ratios and high Cu site densities.

**Bridge adsorption analytics and reaction kinetics.** In the above discussion, we established $\eta_{Cu\cdots Cu}$ and $E_{comp}$ as quantitative descriptors for the atomic structures and adsorption properties of Cu-ZSM5 by combining atomistic simulation, TPR, DFT calculations and NO titration. Now, we show that this analytical information can be used to interpret the catalytic performance of Cu-ZSM5 in the NO

decomposition reaction that takes place at elevated temperatures (>300 °C).

For all five types of Cu-ZSM5, the measured NO conversion exhibited nonlinear behaviour in their dependence on temperature, with the maximum reached at 400–450 °C (Fig. 6a). The decrease in NO conversion at temperatures above 450 °C was not a result of equilibrium shift (Supplementary Fig. 21), neither was it due to catalyst deactivation (Supplementary Fig. 22). Throughout the temperature range investigated here (350–550 °C), the NO conversion decreased as the Si/Al ratio increased. At 450 °C, the NO conversion varied from 85.2% on Cu-ZSM5-11.5 to 46.6% on Cu-ZSM5-30, and to only 2.6% on Cu-ZSM5-100. Both $N_2$ and $N_2O$ were detected as products, and the selectivity towards $N_2$ increased with temperature (Supplementary Fig. 23). The formation of $N_2$ during NO decomposition could be via the reaction shown in equation (7) and the following reactions:

$$[Cu-O-Cu]^{2+} + N_2O \rightarrow [Cu-O_2-Cu]^{2+} + N_2 \quad (8)$$

$$[Cu-O_2-Cu]^{2+} \rightarrow [Cu^+ \cdots Cu^+] + O_2 \quad (9)$$
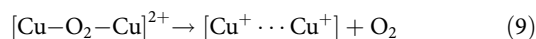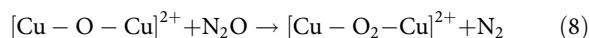
where the reactions shown in equations (8) and (9)[14,15] are required for regeneration of the dimeric Cu sites (Fig. 3a). Among the different catalysts, the zeolites with lower Si/Al ratios have higher $N_2$ selectivity, with Cu-ZSM5-11.5 achieving 99% at 450 °C. It was further found that the zeolite with the higher Cu dimer fraction gives higher specific rates (per Cu site) of $N_2$ formation (Fig. 6b). It can be concluded from these findings that the Cu dimers are active sites for the decomposition of NO to $N_2$. This conclusion was further supported by the comparison of calculated NO decomposition pathways for the two types of Cu site (Fig. 3), which showed that the pathway towards $N_2$ on monomers via the reactions shown in equations (6) and (10) was much less favourable primarily due to the much higher reaction energy of the reaction shown in equation (10) than the one shown in equation (9).

$$[Cu-NO_3]^+ \rightarrow [Cu-NO]^+ + O_2 \quad (10)$$

Noticeably, the $N_2$ selectivity correlated well with the measured $N_2$ evolution from the low-temperature titration experiments (Fig. 6c),

which was expected as the abundance of Cu dimers governs the pathway towards $N_2$ in both cases.

Kinetic measurements were further performed on the Cu-ZSM5 catalysts at reduced loadings. The derived apparent rate constant ($k_{app}$) for $N_2$ formation exhibited a two-stage linear behaviour in the Arrhenius plots (Fig. 6d). In the low-temperature region (for example, $T < 400\,°C$ for Si/Al = 11.5, 20 and 30), $k_{app}$ increased with temperature, indicating a positive activation energy ($E_{app,1} > 0$), whereas an opposite scenery for negative activation energy ($E_{app,2} < 0$) was discerned in the high-temperature region. The maximum $k_{app}$ was also reached at ~400–450 °C, suggesting that the nonlinear dependence of NO conversion on temperature (as shown in Fig. 6a) was a result of kinetic effects[8,40]. Similar to the observation in NO conversion, the Cu-ZSM5 zeolites with lower Si/Al ratios had larger $k_{app}$, in line with the previous reports on Cu-ZSM5 zeolites of the same Si/Al ratio but different Cu exchange levels[17]. According to the kinetic model reported by Modén et al.[8] (see Methods), the two-stage behaviour of Cu-ZSM5 is due to the interplay of NO decomposition (as shown in Fig. 2a) and oxygen evolution pathways, with the latter probably limiting the reaction rate at relatively low temperatures (for example, <400 °C) but becoming feasible at more elevated temperatures. The impact of Cu atomic structures on the reaction kinetics was better visualized by plotting $\ln[k_{app}]$ versus $\eta_{Cu\cdots Cu}$ (Fig. 6e). The nearly linear relationships at both low and high temperatures underline the above conclusion that Cu dimers are the active sites for decomposition of NO to $N_2$. The different slopes (that is, 7.0 at 350 °C versus 3.7 at 550 °C) are indicative of the dissimilar weighing factors of the structure effects on the reaction kinetics, as the low-temperature reaction rate is limited by both NO conversion and oxygen evolution, both of which are more favourable on Cu dimers, whereas the high-temperature rate is only governed by NO conversion that becomes feasible on both dimers and monomers in this condition (for example, at >400 °C). We further found that both $E_{app,1}$ and $E_{app,2}$ correlated well with the adsorption property $\Delta E_{comp}$ derived from the NO titration measurements (Fig. 5f). The direct correlations of these energetic functions are indicative of (and represent an experimental measure of) the underlying scaling relationships among the free energies of various adsorbates and transition states involved in the NO decomposition reaction that are dependent on Cu motif atomic structures (namely, more Cu dimers giving rise to more compression in the $NO_{ad}$ isotherm, reduced energy barriers for NO conversion and more favourable oxygen evolution (compared with Cu monomers)). Moreover, the better linear fitting for the correlation between $E_{app}$ and $\Delta E_{comp}$ than between $E_{app}$ and $\eta_{Cu\cdots Cu}$ (Supplementary Fig. 24) suggests that the secondary structural effects (for example, Cu⋯Cu distance[33,35] and Cu–O–Cu bonding angle[11,16]), as captured by the adsorption compression energy measurements, also propagate to the catalytic reaction kinetics. The successful use of $\eta_{Cu\cdots Cu}$ and $E_{comp}$ to interpret the catalytic performance of Cu-ZSM5 thus bridged the low-temperature adsorption analytics and high-temperature reaction kinetics.

**General applicability of $\eta_{Cu\cdots Cu}$ and $E_{comp}$ as descriptors.** As discussed above, it is clear that $\eta_{Cu\cdots Cu}$ and $E_{comp}$ are valuable descriptors for both the structure and reactivity of Cu-ZSM5. Below, we further show that the established relationships can be generalized to other types of zeolite and reaction.

Similar to Cu-ZSM5, Cu-exchanged mordenite (Cu-MOR) and chabazite (Cu-SSZ13) are also important industrial catalysts that contain Cu dimer active sites[24,45]. We synthesized Cu-MOR-10 and Cu-SSZ13-11, both at full exchange (Cu/Al = ~0.5), for which $\eta_{Cu\cdots Cu}$ was measured to be ~43 and 28%, respectively (Supplementary Fig. 25 and Supplementary Table 11), consistent with the literature results with similar Cu densities (Supplementary Fig. 26)[46,47]. DRIFTS analysis and chemical titration of the reactive adsorption of NO on these two types of Cu-exchanged zeolite (Supplementary

Figs. 27–30 and Supplementary Tables 12–14) confirmed that they also follow the established linear relationships correlating the spectroscopic features (Fig. 4e and Supplementary Fig. 31a), $NO_{ad}$ compression energy (Fig. 5f and Supplementary Fig. 31b) and Cu dimer fraction. Moreover, catalytic studies for NO decomposition indicated that $\eta_{Cu\cdots Cu}$ and $E_{comp}$ quantified for Cu-MOR and Cu-SSZ13 can also describe their reaction kinetics (Supplementary Figs. 32 and 33). The general applicability of these correlations for Cu-exchanged zeolites confirms the established bridges between adsorption analytics and catalytic kinetics and is also in line with the expectation that they are characteristic of the Cu dimer motifs forming on aluminosilicate substrates.

In addition to NO decomposition, we applied $\eta_{Cu\cdots Cu}$ and $E_{comp}$ as descriptors to interpret the kinetics of MTM conversion. Cu-ZSM5 has been extensively studied for the MTM reaction[11,48–50]. Although $[Cu–O–Cu]^{2+}$ has been identified as the active site for methane activation[18], quantitative correlation of the Cu dimer fraction (or number density) with catalytic activity has rarely been reported for MTM. Based on the average Cu site densities recorded in the literature studies[11,49,51], we estimated the corresponding Cu dimer fractions and compression energies using the linear relationships established in Figs. 2d and 5f (see Supplementary Table 15 and Supplementary Fig. 34). The estimated Cu dimer fractions were confirmed by comparing them with the values determined in this study (Supplementary Fig. 35). Linear relationships were thus established between the MTM reactivity and $\eta_{Cu\cdots Cu}$ (Fig. 7a), as well as between the activation energy and $E_{comp}$ (Fig. 7b). To validate the robustness and predictive capability of these relationships, we further performed our own measurements of MTM on Cu-ZSM5-11.5 and Cu-ZSM5-20 (see Methods). These two catalysts produced 18.4 and 13.0 μmol methanol per gram of catalyst at 200 °C, respectively (Supplementary Fig. 36). The corresponding activation energies were determined to be 77.7 and 80.0 kJ mol⁻¹ (Supplementary Fig. 37). Such values are in line with the previous reports with similar Cu site densities (Supplementary Fig. 38)[48,52]. As shown in Fig. 7, the measured catalytic performance fell onto the as-established linear relationships. This thus confirms the general applicability of $\eta_{Cu\cdots Cu}$ and $E_{comp}$ as quantitative descriptors for the MTM reaction.

## Conclusions

We combined atomistic simulation, chemisorption and titration measurements to obtain reaction-relevant structural and property information for Cu-ZSM5. The established descriptors, such as $\eta_{Cu\cdots Cu}$ and $\Delta E_{comp}$, were validated to be applicable to Cu-ZSM5 zeolites prepared in this study and also to other data reported in the literature. They were found to correlate well with the catalytic performance of the Cu-ZSM5 catalysts for NO decomposition. In our studies, we established multiple linear correlations between adsorption analytics and reaction kinetic parameters, which reflect the intrinsic scaling relationships governing the adsorption and catalytic properties of the metal sites within zeolites. These correlations have further been generalized to understand the structure–property relationships of other metal-exchanged zeolites and for interpretation of the catalytic performance of Cu-ZSM5 for methane-to-methanol conversion. The quantitative descriptors and corresponding correlations are thus believed to be valid for guiding the design and development of advanced catalytic materials for various reactions.

## Methods

**Synthesis of Na-ZSM5 with different Si/Al molar ratios.** Na-ZSM5 samples with different Si/Al molar ratios were hydrothermally prepared according to ref. [39], with minor modification of the procedure. Sodium aluminate and sodium hydroxide were dissolved in an aqueous solution of tetrapropylammonium hydroxide, then tetraethylorthosilicate was added. The mixture was stirred until it was uniform. The molar composition of the resulting gel was 4:1:x:20:200 for $Na_2O:Al_2O_3:SiO_2$:tetrapropylammonium hydroxide:$H_2O$, where $x$ was 23, 40, 60, 100 or 200. The gel

was transferred into a Teflon-lined autoclave and crystallized at 150 °C for 3 d. The product was filtered, washed, dried at 100 °C overnight and then calcined in air at 550 °C for 8 h to remove the template. The obtained samples were exchanged in 1 M NaNO₃ solution with a solution-to-zeolite ratio of 10 ml g⁻¹ at 80 °C for 4 h.

**Synthesis of Cu-exchanged zeolites.** The Cu-containing zeolite catalysts were prepared by ion exchange[53]. The Na-containing zeolite precursors with different Si/Al ratios were exchanged in 0.01 M Cu acetate solution at room temperature for 24 h. The amount of Cu²⁺ solution added depended on the Si/Al ratio to ensure a full exchange (that is, Cu/Al ratio = 0.5). The exchange procedure was repeated three times for each zeolite sample. After the third exchange process, the zeolites were filtered, washed thoroughly with at least 4 l deionized water and dried at 100 °C overnight. The as-prepared samples were denoted as Cu-ZSM5-$X(Y)$, where $X$ represents the Si/Al molar ratio measured by X-ray fluorescence spectroscopy and $Y$ represents the Cu/Al molar ratio measured by inductively coupled plasma mass spectrometry.

**Isothermal NO$_{ad}$ measurements.** Isothermal NO$_{ad}$ on Cu-ZSM5 catalysts was conducted in a fixed-bed flow reactor at atmospheric pressure. Before adsorption measurements, the same pretreatment process was applied: 1 g catalyst (40−60 mesh) was loaded into a microflow quartz reactor (7 mm i.d.), heated to 500 °C at a rate of 5 °C min⁻¹ under flowing He (50 ml min⁻¹) and held at 500 °C for 2 h. After pretreatment, the temperature was cooled at 1 °C min⁻¹ down to 80 °C under a pure He atmosphere and the temperature was kept at 80 °C for adsorption measurements. The feed concentrations of NO were adjusted to 300, 500, 800 and 1,500 ppm by mixing pure He and 0.5% NO/He gas. The NO/He mixture (20 l h⁻¹) was fed to the catalyst. The composition of the effluent stream was continuously monitored for the whole length of the experiment until all concentrations of different gas species (NO, N₂O and N₂) were stable. To detect the composition of the effluent stream, an FTIR instrument equipped with a 5-m gas cell and a mercury–cadmium–telluride detector (Nicolet 6700; Thermo Electron), as well as a gas chromatograph equipped with a barrier ionization discharge (BID) detector (GC-2010 Plus; Shimadzu), were employed. The amount of NO adsorbed on the catalyst at the end of the adsorption measurement was evaluated by measuring the overall uptake of NO and the quantities of N₂O, NO₂ and N₂ transiently produced, as follows:

$$NO_{ads} = NO_{uptake} - 2N_2O_{prod} - 2\,N_{2,\,prod} - NO_{hold\,up},  \quad (11)$$

where NO$_{ads}$ represents NO totally adsorbed (as calculated from the mass balance in the gas phase), NO$_{uptake}$ represents the amount of NO consumed (directly measured in the gas phase), N₂O$_{prod}$ represents the amount of N₂O produced (directly measured in the gas phase), N$_{2,\,prod}$ represents the amount of N₂ produced (directly measured in the gas phase) and NO$_{hold\,up}$ represents the amount of NO necessary to fill the dead volumes of the experimental set-up (evaluated in the opportune blank tests). The amounts of these adsorbed species were estimated by integrating the corresponding signals as a function of time. All of these quantities are reported in Supplementary Tables 6–10.

**Analysis of the adsorption isotherm using Ono–Kondo coordinates.** To analyse the adsorption isotherm in the framework of the Ono–Kondo approach[41], consider taking an adsorbate molecule and moving it to the bulk. This is equivalent to the exchange of a molecule with a vacancy,

$$M_a + V \rightarrow V_a + M_b \quad (12)$$

where M is the adsorbate molecule and V is the vacancy that it fills. If this exchange occurs at equilibrium, then:

$$\Delta H - T\Delta S = 0 \quad (13)$$

where $\Delta H$ and $\Delta S$ are the enthalpy and entropy changes and $T$ is the absolute temperature.

Using the Ono–Kondo approach, enthalpy is usually calculated based on certain models (such as lattice geometry and mean-field approximation). Here, we developed a new method allowing the application of Ono–Kondo techniques not only to flat surfaces (macroporous adsorbents) but also for complex morphology, such as in microporous adsorbents. In addition, this new approach is not based on a (mean-field) model of enthalpy for adsorbed molecules. Consider $\Delta H$ in the form of Taylor expansion in powers of density:

$$\frac{\Delta H}{kT} = \frac{\varepsilon_s}{kT} + A_1 x_a + A_2 x_a^2 + A_3 x_a^3 + ... \quad (14)$$

where $A_n = \frac{1}{n!}\frac{\partial^n \Gamma_A}{\partial x_a}$, $\Gamma_A$ is the energy of intermolecular (adsorbate–adsorbate) interactions, $\varepsilon_s$ is the energy of adsorbate–adsorbent interactions and $x_a$ is the average normalized density of the adsorbed phase, representing the ratio of adsorbed amount, $a$, to the adsorption capacity, $a_m$:

$$x_a = \frac{a}{a_m} \quad (15)$$

Note that the local density distribution in the microporous adsorbent can be very complex. However, the measurable value (such as in the adsorption isotherm) is the statistically averaged density, and we define it as an average probability of having an adsorbate molecule in a certain spot of the adsorbed phase.

In the framework of the Ono–Kondo approach[41],

$$\Delta S = k \ln[x_a(1 - x_b)/(1 - x_a)x_b], \quad (16)$$

where $x_b$ is the average normalized density in the bulk. Plugging $\Delta H$ and $\Delta S$ from equations (13) and (16) into equation (13) gives:

$$\ln \frac{x_a(1 - x_b)}{(1 - x_a)x_b} + \frac{\varepsilon_s}{kT} + A_1 x_a + A_2 x_a^2 + A_3 x_a^3 + ... = 0 \quad (17)$$

Equation (17) can be presented as the following form:

$$\ln \frac{x_a(1 - x_b)}{(1 - x_a)x_b} = -\frac{\varepsilon_s}{kT} - x_a \Gamma(x_a), \quad (18)$$

where $\Gamma(x_a) = \Gamma(0) + \frac{1}{2!}\frac{\partial \Gamma}{\partial x_a} x_a + \frac{1}{3!}\frac{\partial^2 \Gamma}{\partial x_a^2} x_a^2 + ...$ and $\Gamma$ is the energy of adsorbate–adsorbate interactions.

As seen from equation (8), plotting

$$Y = \ln \frac{x_a(1 - x_b)}{(1 - x_a)x_b} \quad (19)$$

versus $x_a$ gives information about $\Gamma(x_a)$ (that is, about intermolecular interactions in the adsorbed phase). For example, if the initial slope is negative, there are repulsions between nearest neighbours at small $x_a$, whereas if this slope is positive, there are attractions between nearest neighbours at small $x_a$. For larger $x_a$, the slope can vary and can indicate changes of adsorbate–adsorbate interactions.

As seen from equation (18), the slope in the plot of $Y$ versus $x_a$ gives the energy of lateral interactions, $E_{lat}$, (in units of $kT$) and the intercept gives $\frac{\varepsilon_s}{kT}$. When $E_{lat}$ is negative, it is the energy of adsorption compression, $E_c = E_{lat}$.

For $x_b << 1$ and $x_a << 1$ (when in the range of small densities), equation (19) can be simplified to:

$$Y = \ln \frac{x_a}{x_b} \quad (20)$$

Combining with equation (15), equation (19) can be transformed to:

$$\ln \frac{a}{x_b} = \ln a_m - \frac{\varepsilon_s}{kT} - \frac{\Gamma}{a_m} a \quad (21)$$

Plotting $Y = \ln \frac{a}{x_b}$ versus $a$ gives information about $\Gamma$: the slope gives the energy of adsorption compression and the intercept gives $\frac{\varepsilon_s}{kT}$.

**DFT calculations.** All periodic DFT calculations were performed using the Vienna Ab-initio Simulation Package using a plane-wave cut-off of 500 eV and the Perdew–Burke–Ernzerhof functional. The dispersion interactions were included using the Grimme D3(BJ) scheme. Geometry optimizations were performed until the force on each atom was <0.03 eV Å⁻¹. The initial MFI structure was obtained from the International Zeolite Association (IZA) database and was optimized at a higher plane-wave cut-off of 700 eV to obtain the lattice constants (20.4, 20.1 and 13.4 Å). Due to the large unit cell, all calculations were performed at the Γ point. All calculations included spin polarization. The transition states were determined using a combined climbing image nudged elastic band and dimer approach. Finite differences were used to confirm a single imaginary frequency for the transition state. All free energies were calculated using the harmonic approximation. DFT-optimized geometries of atomistic models are included in Supplementary Data 1.

To minimize the computational cost associated with the high-throughput calculations for the dimer formation energies, the unoptimized MFI structure from the IZA database was used (20.1, 19.7 and 13.1 Å). Only the two Al atoms and the neighbouring O atoms (along with Cu–O–Cu) were allowed to relax, while the other framework Si and O atoms were constrained at their IZA database positions. The formation energy of the dimer was calculated as:
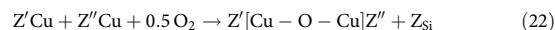
$$Z'Cu + Z''Cu + 0.5\,O_2 \rightarrow Z'[Cu - O - Cu]Z'' + Z_{Si} \quad (22)$$

where $Z'$ and $Z''$ represent one Al substitution in the MFI framework and Z$_{Si}$ represents the energy of an all-silica MFI. We chose this approach to avoid calculations of Z₂[Cu⋯Cu] configurations that required additional efforts to find the lowest energy configurations of the two cations for 2Al atoms in the MFI structure. These assumptions were made to enable the extension of this approach to other zeolite topologies. Even with these assumptions, ~10,000 DFT evaluations were required to generate the [Cu–O–Cu]²⁺ dataset.

**Monte Carlo simulations.** Monte Carlo calculations were performed to determine the distribution of Al atoms. To sufficiently sample the distributions for high Si/Al ratios, a 4 × 4 × 4 supercell was used. To generate the Boltzmann distributions

of Al atoms, the energies for Al substitution associated with each unique T site were obtained from the proton form of the MFI zeolite (Z–H) calculations[54] (see Supplementary Table 2). The Monte Carlo procedure was performed as follows. For a given Si/Al ratio, the necessary Al atoms were randomly inserted into a $4 \times 4 \times 4$ MFI supercell. Each Monte Carlo step consisted of a trial substitution move that replaced an Al atom with an Si atom or an Si atom with an Al atom. The associated trial energy change was obtained from Supplementary Tables 1 and 2 and depended on the T site (T1–T12) of the two atoms. The moves that resulted in lower energy were accepted, while the moves that resulted in an increase in energy were accepted with the standard Boltzmann scheme ($T = 500$ K). Moves that resulted in Al–O–Al bonds were not allowed. To generate random distributions, the energy of Al substitution for every unique T site was assumed to be equal. A total of 100,000 steps were performed to generate ensembles of 500 structures at a given Si/Al ratio.

The ensembles generated from the Monte Carlo simulations were then analysed to classify and count the number of possible Al–Al pairs in the structure. For each structure, the possible Al–Al pairs were ordered according to the formation energy of the corresponding [Cu–O–Cu]$^{2+}$ dimer, with the most favourable [Cu–O–Cu]$^{2+}$/Al–Al pair having the highest priority of dimer formation. Once a pair of Al atoms was assigned as a dimer, they were no longer available to from other dimers. This process was repeated until no further dimers could be formed. To account for the temperature effects, the coverage of each type of dimer was described according to:

$$\vartheta = \frac{\sqrt{p_{O_2}} \times K}{1 + \sqrt{p_{O_2}} \times K} \quad (23)$$

$$K = e^{-\Delta G/(k_B \times T)} \quad (24)$$

The formation energy, $\Delta G$ refers to the energy associated with the formation of the Cu–O–Cu dimer for different relative locations of the Al atoms as:

$$Z'Cu + Z''Cu + 0.5\,O_2 \rightarrow Z'[Cu-O-Cu]Z'' + Z_{Si} \quad (25)$$
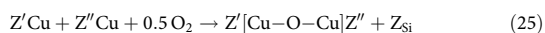
**Catalytic studies.** Catalytic decomposition of NO was conducted in a fixed-bed flow reactor at atmospheric pressure. Before the reaction, a typical pretreatment was applied: 1 g catalyst (40−60 mesh) was loaded into a microflow quartz reactor (7 mm i.d.), heated to 500 °C at a rate of 5 °C min$^{-1}$ under flowing He (50 ml min$^{-1}$) and held at 500 °C for 2 h (the catalyst was self-reduced by spontaneously releasing molecular oxygen). After pretreatment, the temperature was decreased to the desired temperature and the gas flow was then switched to 0.5% NO/He (20 ml min$^{-1}$). The reaction temperature was increased stepwise from 350 to 550 °C, and the reaction was carried out at each temperature until the conversion reached a constant. To determine the conversions of reactants and the formation of products, an FTIR instrument equipped with a 5-m gas cell and a mercury–cadmium–telluride detector (Nicolet 6700; Thermo Electron), as well as a gas chromatograph equipped with a BID detector (GC-2010 Plus; Shimadzu), were employed. Particularly, NO (1,905 cm$^{-1}$), N$_2$O (2,237 cm$^{-1}$) and NO$_2$ (1,630 cm$^{-1}$) were determined by FTIR with a resolution of 8 cm$^{-1}$. N$_2$ was determined by gas chromatography using a HP-POLT Molesieve column. The NO conversion and N$_2$ yield were calculated using the following equations:

$$\text{NO conversion} = \frac{[NO]_{inlet} - [NO]_{outlet}}{[NO]_{inlet}} \times 100\% \quad (26)$$

$$\text{N}_2 \text{ selectivity} = \frac{2[N_2]_{outlet}}{[NO]_{inlet} - [NO]_{outlet}} \times 100\% \quad (27)$$

where [NO]$_{inlet}$ refers to the concentration of NO in the inlet and [NO]$_{outlet}$ and [N$_2$]$_{outlet}$ refer to the concentrations of NO and N$_2$, respectively, in the outlet.

Selective oxidation of MTM was conducted in a fixed-bed flow reactor at atmospheric pressure with all of the tubing heated to 200 °C. The reaction included three consecutive steps: (1) sample activation; (2) CH$_4$ loading; and (3) steam-assisted CH$_3$OH desorption. In a typical experiment, 1 g Cu-ZSM5 or Cu$_2$@CeO$_2$ (40–60 mesh) was activated by calcination in pure O$_2$ flow (20 ml min$^{-1}$) at 400 °C for 1 h. The activated sample was cooled to 200 °C in O$_2$ and flushed by He to remove the physically adsorbed O$_2$ and the O$_2$ in the tubing. In the subsequent CH$_4$ loading step, 90% CH$_4$ in He (20 ml min$^{-1}$) was passed over the catalyst bed for 1 h. A steam-assisted CH$_3$OH desorption step was carried out by passing an equimolar mixture of H$_2$O steam and He (20 ml min$^{-1}$) through the catalyst bed for 2 h. The reaction products were identified and quantified using a gas chromatograph equipped with a BID detector (GC-2010 Plus; Shimadzu).

**Kinetic measurements.** To obtain the kinetic data of NO decomposition over different Cu-ZSM5 zeolites, 50−400 mg fresh catalyst (40−60 mesh) was loaded into a microflow quartz reactor. The catalyst was pretreated using the same procedure as above. Experiments were conducted at ambient pressure and in the temperature range of 300–550 °C. Similarly, an FTIR instrument equipped with

gas cell and a gas chromatograph equipped with a BID detector were applied to monitor the concentrations of NO, N$_2$O, NO$_2$ and N$_2$ from the outlet.

According to the work of by Modén et al.[8], the rate equations of direct NO decomposition in the full range of reaction temperatures (300–600 °C) can be expressed as:

$$r = \frac{k_{NO}[NO]^2}{1 + k_{O_2}[O_2]^{1/2}} \quad (28)$$

At low temperature, due to the high coverage of [O]$^*$, the $k_{O_2}[O_2]^{1/2}$ term in the denominator of equation (28) becomes larger than 1 and the rate approaches the expression of the form $r = \frac{k_{NO}[NO]^2}{k_{O_2}[O_2]^{1/2}}$; for this rate expression, the apparent rate constant $k_{app,1} = k_{NO}/k_{O_2}$.

At high temperature, due to the coverage of [O]$^*$ decreasing with the temperature, the term $k_{O_2}[O_2]^{1/2}$ becomes much smaller than 1, and the rate approaches the expression of the form $r = k_{NO}[NO]^2$; for this rate expression, the apparent rate constant $k_{app,2} = k_{NO}$.

Per the rate expressions above, the apparent rate constants at low and high temperatures can be calculated out, then plotted against the reciprocal temperature, leading to the Arrhenius plots of NO decomposition over different Cu-ZSM5 catalysts. Thus, the apparent activation energy ($E_{app}$) can be obtained from the slopes in the Arrhenius plots.

To obtain the kinetic data for selective oxidation of CH$_4$ over different Cu-ZSM5 zeolites and Cu$_2$@CeO$_2$, the reactions were conducted at 150, 175 and 200 °C with other conditions consistent.

## Data availability
The data that support the findings of this study are available on the Figshare platform at https://doi.org/10.6084/m9.figshare.13128506.v1 (ref. [55]). Source data are provided with this paper.

## References
1. Yang, J. C., Small, M. W., Grieshaber, R. V. & Nuzzo, R. G. Recent developments and applications of electron microscopy to heterogeneous catalysis. *Chem. Soc. Rev.* **41**, 8179–8194 (2012).
2. Bordiga, S., Groppo, E., Agostini, G., van Bokhoven, J. A. & Lamberti, C. Reactivity of surface species in heterogeneous catalysts probed by in situ X-ray absorption techniques. *Chem. Rev.* **113**, 1736–1850 (2013).
3. Zaera, F. New advances in the use of infrared absorption spectroscopy for the characterization of heterogeneous catalytic reactions. *Chem. Soc. Rev.* **43**, 7624–7663 (2014).
4. Wachs, I. E. & Roberts, C. A. Monitoring surface metal oxide catalytic active sites with Raman spectroscopy. *Chem. Soc. Rev.* **39**, 5002–5017 (2010).
5. Norskov, J. K., Bligaard, T., Rossmeisl, J. & Christensen, C. H. Towards the computational design of solid catalysts. *Nat. Chem.* **1**, 37–46 (2009).
6. Zhang, R. D., Liu, N., Lei, Z. G. & Chen, B. H. Selective transformation of various nitrogen-containing exhaust gases toward N$_2$ over zeolite catalysts. *Chem. Rev.* **116**, 3658–3721 (2016).
7. Lamberti, C. et al. XAFS, IR, and UV-vis study of the Cu$^I$ environment in Cu$^I$-ZSM-5. *J. Phys. Chem. B* **101**, 344–360 (1997).
8. Moden, B., Da Costa, P., Fonfe, B., Lee, D. K. & Iglesia, E. Kinetics and mechanism of steady-state catalytic NO decomposition reactions on Cu-ZSM5. *J. Catal.* **209**, 75–86 (2002).
9. Snyder, B. E. R., Bols, M. L., Schoonheydt, R. A., Sels, B. F. & Solomon, E. I. Iron and copper active sites in zeolites and their correlation to metalloenzymes. *Chem. Rev.* **118**, 2718–2768 (2018).
10. Giordanino, F. et al. Characterization of Cu-exchanged SSZ-13: a comparative FTIR, UV-Vis, and EPR study with Cu-ZSM-5 and Cu-β with similar Si/Al and Cu/Al ratios. *Dalton Trans.* **42**, 12741–12761 (2013).
11. Woertink, J. S. et al. A [Cu$_2$O]$^{2+}$ core in Cu-ZSM-5, the active site in the oxidation of methane to methanol. *Proc. Natl Acad. Sci. USA* **106**, 18908–18913 (2009).
12. Groothaert, M. H., Pierloot, K., Delabie, A. & Schoonheydt, R. A. Identification of Cu(II) coordination structures in Cu-ZSM-5, based on a DFT/ab initio assignment of the EPR spectra. *Phys. Chem. Chem. Phys.* **5**, 2135–2144 (2003).
13. Groothaert, M. H., van Bokhoven, J. A., Battiston, A. A., Weckhuysen, B. M. & Schoonheydt, R. A. Bis(μ-oxo)dicopper in Cu-ZSM-5 and its role in the decomposition of NO: a combined in situ XAFS, UV−vis−near-IR, and kinetic study. *J. Am. Chem. Soc.* **125**, 7629–7640 (2003).
14. Sajith, P. K., Shiota, Y. & Yoshizawa, K. Role of acidic proton in the decomposition of NO over dimeric Cu(I) active sites in Cu-ZSM-5 catalyst: a QM/MM study. *ACS Catal.* **4**, 2075–2085 (2014).
15. Moretti, G. et al. Dimeric Cu(I) species in Cu-ZSM-5 catalysts: the active sites for the NO decomposition. *J. Catal.* **232**, 476–487 (2005).

16. Tsai, M. L. et al. [Cu$_2$O]$^{2+}$ active site formation in Cu-ZSM-5: geometric and electronic structure requirements for N$_2$O activation. *J. Am. Chem. Soc.* **136**, 3522–3529 (2014).

17. Da Costa, P., Moden, B., Meitzner, G. D., Lee, D. K. & Iglesia, E. Spectroscopic and chemical characterization of active and inactive Cu species in NO decomposition catalysts based on Cu-ZSM5. *Phys. Chem. Chem. Phys.* **4**, 4590–4601 (2002).

18. Ravi, M. et al. Misconceptions and challenges in methane-to-methanol over transition-metal-exchanged zeolites. *Nat. Catal.* **2**, 485–494 (2019).

19. Kustova, M. Y., Rasmussen, S. B., Kustov, A. L. & Christensen, C. H. Direct NO decomposition over conventional and mesoporous Cu-ZSM-5 and Cu-ZSM-11 catalysts: improved performance with hierarchical zeolites. *Appl. Catal. B* **67**, 60–67 (2006).

20. Xie, P. F. et al. CoZSM-11 catalysts for N$_2$O decomposition: effect of preparation methods and nature of active sites. *Appl. Catal. B* **170**, 34–42 (2015).

21. Fanning, P. E. & Vannice, M. A. A DRIFTS study of Cu-ZSM-5 prior to and during its use for N$_2$O decomposition. *J. Catal.* **207**, 166–182 (2002).

22. Beutel, T., Sarkany, J., Lei, G. D., Yan, J. Y. & Sachtler, W. M. H. Redox chemistry of Cu/ZSM-5. *J. Phys. Chem.* **100**, 845–851 (1996).

23. Loewenstein, W. The distribution of aluminum in the tetrahedra of silicates and aluminates. *Am. Mineral.* **39**, 92–96 (1954); http://www.minsocam.org/ammin/AM39/AM39_92.pdf

24. Paolucci, C. et al. Dynamic multinuclear sites formed by mobilized copper ions in NO$_x$ selective catalytic reduction. *Science* **357**, 898–903 (2017).

25. Latimer, A. A. et al. Understanding trends in C–H bond activation in heterogeneous catalysis. *Nat. Mater.* **16**, 225–229 (2017).

26. Zhao, Z. J., Kulkarni, A., Vilella, L., Norskov, J. K. & Studt, F. Theoretical insights into the selective oxidation of methane to methanol in copper-exchanged mordenite. *ACS Catal.* **6**, 3760–3766 (2016).

27. Larsen, A. H. et al. The atomic simulation environment—a Python library for working with atoms. *J. Phys. Condens. Matter* **29**, 273002 (2017).

28. Wang, S., He, Y., Jiao, W. Y., Wang, J. G. & Fan, W. B. Recent experimental and theoretical studies on Al siting/acid site distribution in zeolite framework. *Curr. Opin. Chem. Eng.* **23**, 146–154 (2019).

29. Itadani, A. et al. New information related to the adsorption model of N$_2$ on CuMFI at room temperature. *J. Phys. Chem. C* **111**, 16701–16705 (2007).

30. Henriques, C. et al. An FT-IR study of NO adsorption over Cu-exchanged MFI catalysts: effect of Si/Al ratio, copper loading and catalyst pre-treatment. *Appl. Catal. B* **16**, 79–95 (1998).

31. Kosinov, N., Liu, C., Hensen, E. J. M. & Pidko, E. A. Engineering of transition metal catalysts confined in zeolites. *Chem. Mater.* **30**, 3177–3198 (2018).

32. Agarwal, N. et al. Aqueous Au–Pd colloids catalyze selective CH$_4$ oxidation to CH$_3$OH with O$_2$ under mild conditions. *Science* **358**, 223–226 (2017).

33. Schneider, W. F., Hass, K. C., Ramprasad, R. & Adams, J. B. First-principles analysis of elementary steps in the catalytic decomposition of NO by Cu-exchanged zeolites. *J. Phys. Chem. B* **101**, 4353–4357 (1997).

34. Fanson, P. T., Stradt, M. W., Lauterbach, J. & Delgass, W. N. The effect of Si/Al ratio and copper exchange level on isothermal kinetic rate oscillations for N$_2$O decomposition over Cu-ZSM-5: a transient FTIR study. *Appl. Catal. B* **38**, 331–347 (2002).

35. Hadjiivanov, K. I. Identification of neutral and charged N$_x$O$_y$ surface species by IR spectroscopy. *Catal. Rev.* **42**, 71–144 (2000).

36. Morpurgo, S. A. DFT study on the mechanism of NO decomposition catalyzed by short-distance Cu(I) pairs in Cu-ZSM-5. *Mol. Catal.* **434**, 96–105 (2017).

37. Izquierdo, R., Rodriguez, L. J., Anez, R. & Sierraalta, A. Direct catalytic decomposition of NO with Cu-ZSM-5: a DFT-ONIOM study. *J. Mol. Catal. A Chem.* **348**, 55–62 (2011).

38. Konduru, M. V. & Chuang, S. S. C. Investigation of adsorbate reactivity during NO decomposition over different levels of copper ion-exchanged ZSM-5 using in situ IR technique. *J. Phys. Chem. B* **103**, 5802–5813 (1999).

39. Kuroda, Y., Kumashiro, R., Yoshimoto, T. & Nagao, M. Characterization of active sites on copper ion-exchanged ZSM-5-type zeolite for NO decomposition reaction. *Phys. Chem. Chem. Phys.* **1**, 649–656 (1999).

40. Lee, D. K. Thermodynamic features of the Cu-ZSM-5 catalyzed NO decomposition reaction. *Korean J. Chem. Eng.* **23**, 547–554 (2006).

41. Aranovich, G. L. & Donohue, M. D. Phase loops in density-functional-theory calculations of adsorption in nanoscale pores. *Phys. Rev. E* **60**, 5552–5560 (1999).

42. Aranovich, G. L. & Donohue, M. D. Adsorption compression: an important new aspect of adsorption behavior and capillarity. *Langmuir* **19**, 2722–2735 (2003).

43. Smeets, P. J. et al. Direct NO and N$_2$O decomposition and NO-assisted N$_2$O decomposition over Cu-zeolites: elucidating the influence of the Cu–Cu distance on oxygen migration. *J. Catal.* **245**, 358–368 (2007).

44. Teraishi, K. et al. Active site structure of Cu/ZSM-5: computational study. *J. Phys. Chem. B* **101**, 8079–8085 (1997).

45. Sushkevich, V. L., Palagin, D., Ranocchiari, M. & van Bokhoven, J. A. Selective anaerobic oxidation of methane enables direct synthesis of methanol. *Science* **356**, 523–527 (2017).

46. Verma, A. A. et al. NO oxidation: a probe reaction on Cu-SSZ-13. *J. Catal.* **312**, 179–190 (2014).

47. Pappas, D. K. et al. The nuclearity of the active site for methane to methanol conversion in Cu-mordenite: a quantitative assessment. *J. Am. Chem. Soc.* **140**, 15270–15278 (2018).

48. Narsimhan, K., Iyoki, K., Dinh, K. & Roman-Leshkov, Y. Catalytic oxidation of methane into methanol over copper-exchanged zeolites with oxygen at low temperature. *ACS Cent. Sci.* **2**, 424–429 (2016).

49. Groothaert, M. H., Smeets, P. J., Sels, B. F., Jacobs, P. A. & Schoonheydt, R. A. Selective oxidation of methane by the bis(μ-oxo)dicopper core stabilized on ZSM-5 and mordenite zeolites. *J. Am. Chem. Soc.* **127**, 1394–1395 (2005).

50. Kulkarni, A. R., Zhao, Z. J., Siahrostami, S., Norskov, J. K. & Studt, F. Cation-exchanged zeolites for the selective oxidation of methane to methanol. *Catal. Sci. Technol.* **8**, 114–123 (2018).

51. Yumura, T., Hirose, Y., Wakasugi, T., Kuroda, Y. & Kobayashi, H. Roles of water molecules in modulating the reactivity of dioxygen-bound Cu-ZSM-5 toward methane: a theoretical prediction. *ACS Catal.* **6**, 2487–2495 (2016).

52. Tomkins, P. et al. Isothermal cyclic conversion of methane into methanol over copper-exchanged zeolite at low temperature. *Angew. Chem. Int. Ed.* **55**, 5467–5471 (2016).

53. Xie, P. F. et al. Catalytic decomposition of N$_2$O over Cu-ZSM-11 catalysts. *Microporous Mesoporous Mater.* **191**, 112–117 (2014).

54. Xing, B., Ma, J. H., Li, R. F. & Jiao, H. J. Location, distribution and acidity of Al substitution in ZSM-5 with different Si/Al ratios—a periodic DFT computation. *Catal. Sci. Tech.* **7**, 5694–5708 (2017).

55. Xie, P. F. et al. Bridging adsorption analytics and catalytic kinetics for metal-exchanged zeolites. *Figshare* https://doi.org/10.6084/m9.figshare.13128506.v1 (2020).

## Author contributions

C.W. and P.X. conceived of the idea and experimental design. P.X. and T.P. carried out the experiments. P.X. and C.W. wrote the paper. M.D. and G.A. contributed to analysis of the NO$_{ad}$ isotherms using Ono–Kondo coordinates. A.K. and J.G. performed DFT calculations for this work. All of the authors discussed the results and contributed to manuscript preparation.

## Competing interests

The authors declare no competing interests.

## Additional information

**Supplementary information** is available for this paper at https://doi.org/10.1038/s41929-020-00555-0.

**Correspondence and requests for materials** should be addressed to A.K. or C.W.

**Peer review information** *Nature Catalysis* thanks Dennis Palagin and the other, anonymous, reviewer(s) for their contribution to the peer review of this work.

**Reprints and permissions information** is available at www.nature.com/reprints.

**Publisher's note** Springer Nature remains neutral with regard to jurisdictional claims in published maps and institutional affiliations.